Supplemental Material for: Dissipative Topological Phase Transition with Strong System-Environment Coupling

Wei Nie,[1] Mauro Antezza,[2,3] Yu-xi Liu,[4,5,*] and Franco Nori[1,6,7,†]

[1] *Theoretical Quantum Physics Laboratory, RIKEN Cluster for Pioneering Research, Wako-shi, Saitama 351-0198, Japan*
[2] *Laboratoire Charles Coulomb (L2C), UMR 5221 CNRS-Université de Montpellier, F- 34095 Montpellier, France*
[3] *Institut Universitaire de France, 1 rue Descartes, F-75231 Paris Cedex 05, France*
[4] *School of Integrated Circuits, Tsinghua University, Beijing 100084, China*
[5] *Frontier Science Center for Quantum Information, Beijing, China*
[6] *RIKEN Center for Quantum Computing (RQC), 2-1 Hirosawa, Wako-shi, Saitama 351-0198, Japan*
[7] *Physics Department, The University of Michigan, Ann Arbor, Michigan 48109-1040, USA*

In this Supplemental Material, we present details about the results in the main text.

(I) MASTER EQUATION OF A TOPOLOGICAL EMITTER ARRAY IN AN ELECTROMAGNETIC ENVIRONMENT

Figure S1(a) shows a topological emitter array coupled to an electromagnetic environment. The photon exchange between the emitter array and the environment leads to interaction between emitters. The environment-induced interaction yields nontrivial effects to the topological emitter array. Here, we show how to derive the master equation of the system. The Hamiltonian of the whole system is

$$H = H_{\mathrm{S}} + H_{\mathrm{E}} + H_{\mathrm{SE}}. \tag{S1}$$

The Hamiltonian of the emitter array is $H_{\mathrm{S}} = H_0 + H_{\mathrm{topo}}$, where $H_0 = \sum_i \hbar\omega_0 \sigma_i^+ \sigma_i$ and

$$H_{\mathrm{topo}} = \sum_i \hbar J_i \sigma_i^+ \sigma_{i+1}^- + \mathrm{H.c.} \tag{S2}$$

Here, σ_i^+ (σ_i^-) is the arising (decreasing) operator of the ith emitter. The interaction between emitters is given by $J_i = J_1$ (J_2) for odd (even) value of i. The energy spectrum of the topological emitter array is shown in Fig. S1(b). Due to topological protection, the degenerate edge states have frequency ω_0, as the same as the frequency of a single emitter. The spectrum width $\Delta\omega$ characterizes the energy scale of the emitter array in single-excitation subspace. The Hamiltonian for the electromagnetic environment is

$$H_{\mathrm{E}} = \int d^3\boldsymbol{r} \int_{\omega_-}^{\omega_+} d\omega\, \hbar\omega\, \hat{\boldsymbol{a}}^\dagger(\boldsymbol{r},\boldsymbol{\omega})\hat{\boldsymbol{a}}(\boldsymbol{r},\omega), \tag{S3}$$

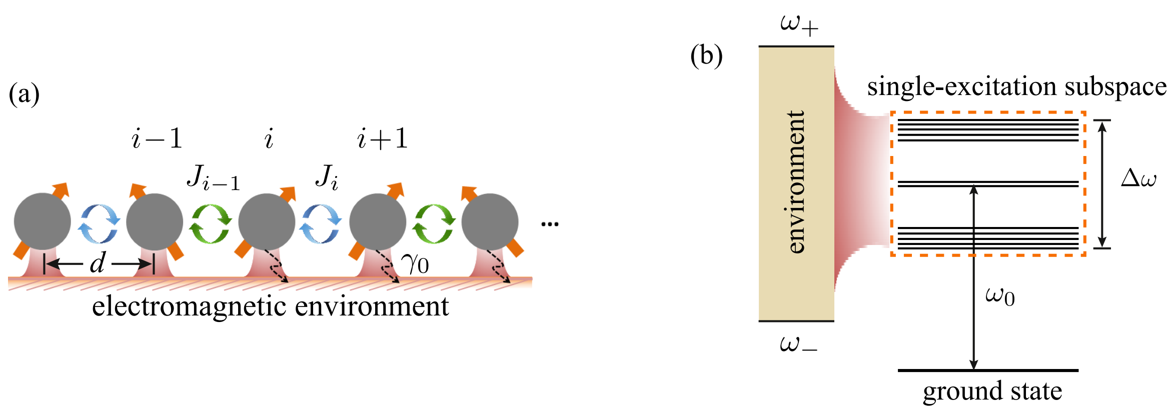

FIG. S1. (a) Schematic of a topological emitter array coupled to an electromagnetic environment. (b) Coupling between the topological emitter array and the electromagnetic environment in the frequency regime. The spectrum width $\Delta\omega$ of the emitter array is assumed to be much smaller than the width $(\omega_+ - \omega_-)$ of the photonic band. Here, ω_- and ω_+ are lower and upper bounds of photonic frequencies in the environment.

where $\hat{\boldsymbol{a}}^\dagger(\boldsymbol{r},\omega)$ ($\hat{\boldsymbol{a}}(\boldsymbol{r},\omega)$) represents the creation (annihilation) operator of photons in the electromagnetic environment. Here, ω_- and ω_+ denote the lower and upper frequency bounds of photonic modes in the electromagnetic environment. Spectrum width $\Delta\omega$ of the emitter array and bandwidth $(\omega_+ - \omega_-)$ are characteristic energy scales of the system. In this work, we are interested in how the electromagnetic environment with continuous photonic modes affects topological properties. Without loss of generality, we assume the broadband photonic modes with $\omega_- = 0$ and $\omega_+ = \infty$. Moreover, the spectrum width is much smaller than the emitter frequency, i.e., $\Delta\omega \ll \omega_0$. The interaction between the emitters and the environment is

$$H_{\mathrm{SE}} = -\sum_i \int_0^\infty d\omega \left(\hat{\boldsymbol{d}}_i \cdot \boldsymbol{E}(\boldsymbol{r}_i,\omega) + \mathrm{H.c.}\right), \tag{S4}$$

with dipole moment operators $\hat{\boldsymbol{d}}_i = \boldsymbol{d}_i\sigma_i^- + \boldsymbol{d}_i^*\sigma_i^+$, and electric field $\boldsymbol{E}(\boldsymbol{r},\omega) = i\eta \int d^3\boldsymbol{r}' \sqrt{\varepsilon_I(\boldsymbol{r}',\omega)}\boldsymbol{G}(\boldsymbol{r},\boldsymbol{r}',\omega)\hat{a}(\boldsymbol{r}',\omega)$. Here, ε_I is the imaginary part of the permittivity; $\boldsymbol{G}(\boldsymbol{r},\boldsymbol{r}',\omega)$ is the electric field response at $\boldsymbol{r}$ to a point source at $\boldsymbol{r}'$. The dynamics of the whole system is described by

$$\dot{\rho} = -\frac{i}{\hbar}[H,\rho], \tag{S5}$$

where ρ is the density matrix of the entire system. In the interaction picture $U = \exp[-i(H_0 + H_{\mathrm{E}})t/\hbar]$, we have

$$\dot{\rho}_{\mathrm{int}} = -\frac{i}{\hbar}[H_{\mathrm{topo}} + H_{\mathrm{SE,int}}, \rho_{\mathrm{int}}], \tag{S6}$$

with the interaction Hamiltonian

$$H_{\mathrm{SE,int}}(t) = -\sum_i \int_0^\infty d\omega \left(\sigma_i^+ \boldsymbol{d}_i^* \cdot \boldsymbol{E}(\boldsymbol{r}_i,\omega)e^{-i(\omega-\omega_0)t} + \mathrm{H.c.}\right), \tag{S7}$$

in the rotating wave approximation. By formally integrating Eq. (S6), we obtain

$$\rho_{\mathrm{int}} = \rho_{S,\mathrm{int}}(0) \bigotimes \rho_{\mathrm{E0}} - \frac{i}{\hbar}\int_0^t dt'[H_{\mathrm{topo}} + H_{\mathrm{SE,int}}(t'), \rho_{\mathrm{int}}(t')], \tag{S8}$$

where $\rho_{\mathrm{S,int}}(0)$ and ρ_{E0} represent the initial density matrices for the topological emitter array and environment, respectively. By tracing over photonic modes of the environment in Eq. (S6), we have

$$\dot{\rho}_{\mathrm{S,int}} = -\frac{i}{\hbar}[H_{\mathrm{topo}}, \rho_{\mathrm{S,int}}] - \frac{i}{\hbar}\mathrm{Tr}_{\mathrm{E}}\{[H_{\mathrm{SE,int}}, \rho_{\mathrm{int}}]\}, \tag{S9}$$

where $\rho_{\mathrm{S,int}}$ represents the density matrix of the emitter array. Replacing ρ_{int} with Eq. (S8), we obtain

$$\dot{\rho}_{\mathrm{S,int}} = -\frac{i}{\hbar}[H_{\mathrm{topo}}, \rho_{\mathrm{S,int}}] - \frac{1}{\hbar^2}\int_0^t dt'\mathrm{Tr}_{\mathrm{E}}\{[H_{\mathrm{SE,int}}(t), [H_{\mathrm{topo}} + H_{\mathrm{SE,int}}(t'), \rho_{\mathrm{int}}(t')]]\}. \tag{S10}$$

We have assumed that the mean initial system-environment (SE) coupling is zero. At first, we consider the Born approximation, which assumes that the coupling between emitters and the electromagnetic environment is weak, such that the influence of emitters on the environment is small. As a consequence, the density matrix of the environment is only negligibly affected by the emitter-environment coupling. The state of the whole system can be approximately expressed as $\rho_{\mathrm{int}}(t) \approx \rho_{\mathrm{S,int}}(t) \otimes \rho_{\mathrm{E0}}$. The evolution of the density matrix only depends on its current state under the Markov approximation [S1].

The Born-Markov approximation can be guaranteed by the condition that the relaxation time of the environment is much faster than the time scale over which the state of the emitter array varies. Thus, the environment does not have a memory effect.

At last, we make a second Markov approximation, extending the upper limit of the time integral to infinity. With the Born-Markov approximation, and after changing the time variable to $t' = t - \tau$, we obtain

$$\dot{\rho}_{\mathrm{S,int}} = -\frac{i}{\hbar}[H_{\mathrm{topo}}, \rho_{\mathrm{S,int}}] - \frac{1}{\hbar^2}\int_0^\infty d\tau \mathrm{Tr}_{\mathrm{E}}\{[H_{\mathrm{SE,int}}(t), [H_{\mathrm{topo}} + H_{\mathrm{SE,int}}(t-\tau), \rho_{\mathrm{S,int}}(t)\rho_{\mathrm{E0}}]]\}. \tag{S11}$$

Here, we have replaced $\rho_{S,\text{int}}(t-\tau)$ with $\rho_{S,\text{int}}(t)$ by ignoring the memory effect due to the Born-Markov approximation. It is easy to find that $\text{Tr}_{\text{E}}\{[H_{\text{SE,int}}(t), [H_{\text{topo}}, \rho_{\text{S,int}}(t)\rho_{\text{E0}}]]\} = 0$ for the vacuum electromagnetic fields, i.e., $\langle \hat{a}(\boldsymbol{r}, \omega)\rangle = 0$. The commutator in the second term of the above equation becomes

$$\begin{aligned} &H_{\text{SE,int}}(t)H_{\text{SE,int}}(t-\tau)\rho_{\text{S,int}}(t)\rho_{\text{E0}} - H_{\text{SE,int}}(t-\tau)\rho_{\text{S,int}}(t)\rho_{\text{E0}}H_{\text{SE,int}}(t) \\ &-H_{\text{SE,int}}(t)\rho_{\text{S,int}}(t)\rho_{\text{E0}}H_{\text{SE,int}}(t-\tau) + \rho_{\text{S,int}}(t)\rho_{\text{E0}}H_{\text{SE,int}}(t-\tau)H_{\text{SE,int}}(t). \end{aligned} \tag{S12}$$

For the first term,

$$\begin{aligned} \text{Tr}_{\text{E}}\{[H_{\text{SE,int}}(t)H_{\text{SE,int}}(t-\tau)\rho_{\text{S,int}}(t)\rho_{\text{E0}}]\} = \sum_{i,j} \boldsymbol{d}_i^* \boldsymbol{d}_j \int_0^\infty d\omega e^{i(\omega_0-\omega)\tau}\sigma_i^\dagger(t)\sigma_j^-(t-\tau)\rho_{\text{S,int}} \\ \times \text{Tr}_{\text{E}}\{\boldsymbol{E}(\boldsymbol{r}_i,\omega)\boldsymbol{E}^\dagger(\boldsymbol{r}_j,\omega)\rho_{\text{E0}}\}. \end{aligned} \tag{S13}$$

Note that the emitter operators $\sigma_i^\pm$ are slowly varying since $J_{1,2} \ll \omega$. Therefore, $\sigma_j^-(t-\tau) \approx \sigma_j^-(t)$. It can be shown that

$$\begin{aligned} \text{Tr}_{\text{E}}\{\boldsymbol{E}(\boldsymbol{r}_i,\omega)\boldsymbol{E}^\dagger(\boldsymbol{r}_j,\omega)\rho_{\text{E0}}\} &= \frac{\hbar\omega^4}{\pi\varepsilon_0 c^4}\int d^3\boldsymbol{r}\varepsilon_I \boldsymbol{G}(\boldsymbol{r}_i,\boldsymbol{r},\omega)\boldsymbol{G}^\dagger(\boldsymbol{r}_j,\boldsymbol{r},\omega) \\ &= \frac{\hbar}{\pi\varepsilon_0}\frac{\omega^2}{c^2}\text{Im}[\boldsymbol{G}(\boldsymbol{r}_i,\boldsymbol{r}_j,\omega)]. \end{aligned} \tag{S14}$$

In deriving Eqs. (S13) and (S14), we have used $\text{Tr}_{\text{E}}\{\hat{a}(r,\omega)\hat{a}^\dagger(r',\omega')\rho_{\text{E0}}\} = \delta(r-r')\delta(\omega-\omega')$ and the property [S2]

$$2i\frac{\omega^2}{c^2}\int d^3\boldsymbol{r}''\varepsilon_I\boldsymbol{G}(\boldsymbol{r},\boldsymbol{r}'',\omega)\boldsymbol{G}^\dagger(\boldsymbol{r}',\boldsymbol{r}'',\omega) = \boldsymbol{G}(\boldsymbol{r},\boldsymbol{r}',\omega) - \boldsymbol{G}^*(\boldsymbol{r},\boldsymbol{r}',\omega). \tag{S15}$$

Therefore,

$$\begin{aligned} \int_0^\infty d\tau \text{Tr}_{\text{E}}\{H_{\text{SE,int}}(t)H_{\text{SE,int}}(t-\tau)\rho_{\text{S,int}}(t)\rho_{\text{E0}}\} = \frac{\hbar}{\pi\varepsilon_0 c^2}\sum_{i,j}\sigma_i^+(t)\sigma_j^-(t)\rho_{\text{S,int}}(t)\int_0^\infty \omega^2 d\omega \\ \times \int_0^\infty d\tau e^{i(\omega_0-\omega)\tau}\boldsymbol{d}_i^*\text{Im}[\boldsymbol{G}(\boldsymbol{r}_i,\boldsymbol{r}_j,\omega)]\boldsymbol{d}_j. \end{aligned} \tag{S16}$$

We can do the same calculation for other three terms in Eq. (S12). Therefore, the dynamic equation of $\rho_{\text{SE,int}}(t)$ is derived by means of time integral over τ. After transforming Eq. (S11) to the Schrödinger picture, we obtain the master equation

$$\dot{\rho}(t) = -\frac{i}{\hbar}[H_0 + H_{\text{topo}} + H_{\text{ph}}, \rho(t)] + \mathcal{D}[\rho], \tag{S17}$$

with

$$H_{\text{ph}} = \sum_{i,j=1}^N \hbar g_{ij}(\sigma_i^-\sigma_j^+ + \sigma_j^-\sigma_i^+), \tag{S18}$$

$$\mathcal{D}[\rho] = \sum_{i,j=1}^N \gamma_{ij}(\sigma_i^-\rho\sigma_j^+ - \frac{1}{2}\sigma_i^+\sigma_j^-\rho - \frac{1}{2}\rho\sigma_i^+\sigma_j^-). \tag{S19}$$

The environment-induced interaction and dissipation are

$$g_{ij} = \frac{\omega_0^2}{\hbar\varepsilon_0 c^2}\text{Re}[\boldsymbol{d}_i^*\cdot\boldsymbol{G}(\boldsymbol{r}_i,\boldsymbol{r}_j,\omega_0)\cdot\boldsymbol{d}_j], \tag{S20}$$

$$\gamma_{ij} = \frac{2\omega_0^2}{\hbar\varepsilon_0 c^2}\text{Im}[\boldsymbol{d}_i^*\cdot\boldsymbol{G}(\boldsymbol{r}_i,\boldsymbol{r}_j,\omega_0)\cdot\boldsymbol{d}_j], \tag{S21}$$

respectively.

(II) TOPOLOGICAL PHASE TRANSITION IN THE COHERENT INTERACTION

The electromagnetic environment produces long-range interactions and correlated dissipations between emitters. We find that the coherent interaction $H = H_{\text{topo}} + H_{\text{ph}}$ exhibits translational symmetry when the spacing between nearest neighboring emitters is properly chosen. This feature allows us to study the topological property of the environment-coupled emitter array.

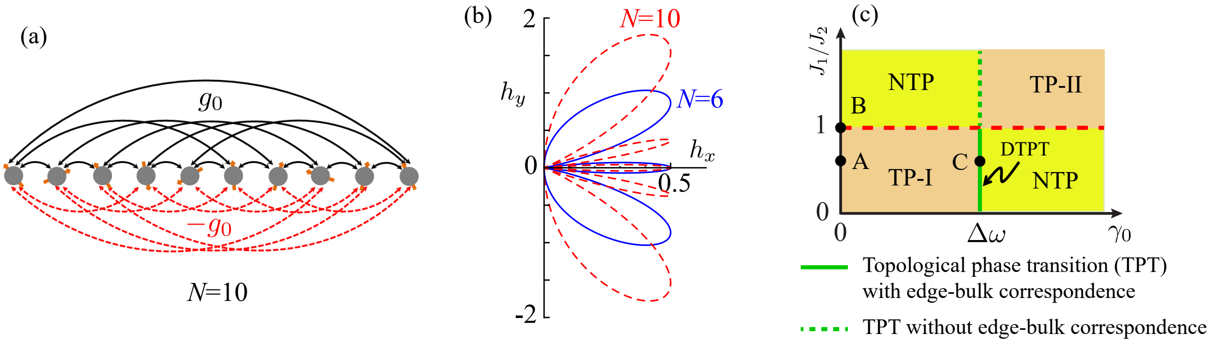

FIG. S2. (a) Environment-induced interaction for the emitter array with $d = 3\lambda_0/4$ and $N = 10$. Here, $g_0 = -\gamma_0/2$. The black-solid and red-dashed curves correspond to g_0 and $-g_0$, respectively. (b) Topologies for emitter arrays with different sizes. The blue-solid and red-dashed curves correspond to emitter arrays with $N = 6$ and $N = 10$, respectively. (c) Phase diagram of systems with even numbers of emitters. We consider open boundary conditions in the dimerized interaction. TP-I is the topological phase with edge states, TP-II is the topological phase without edge state, NTP denotes the non-topological phase. The topological phase is protected by the SSH criticality and dissipative topological phase transition from the non-topological phase.

(II-A) Topological phase transition via chiral symmetry: analytical method

In the main text we consider the topology in auxiliary space for an emitter array with $N = 6$. For the emitter arrays $N = 6+4n$ (with $n = 0, 1, 2, \ldots$), the translational symmetry is preserved for photon-mediated long-range interactions. In Fig. S2(a), we show the photon-mediated interaction for an emitter array with $N = 10$. Translational symmetry is found for the nearest neighboring interaction $i \leftrightarrow (i+1)$ and long-range interaction $i \leftrightarrow (i+9)$ with the effective interaction $g_0/2$. The long-range interaction $i \leftrightarrow (i+5)$ is also translationally invariant with the effective interaction $g_0/2$. Similarly, the long-range interactions $i \leftrightarrow (i+3)$ and $i \leftrightarrow (i+7)$ preserve the translational symmetry for the effective interaction $-g_0/2$. Therefore, the translational symmetry is preserved for all interaction ranges. With the Fourier transformation $\sigma^+_{A,k} = \sum_n e^{iknd}\sigma^+_{A,n}$, $\sigma^+_{B,k} = \sum_n e^{iknd}\sigma^+_{B,n}$, where n labels the nth unit cell of the topological emitter array, we can obtain the Hamiltonian in the quasi-momentum space. The Hamiltonian in momentum space for the emitter array with $N = 10$ is $\mathcal{H}(k) = h_x(k)\tau_x + h_y(k)\tau_y$, with

$$h_x(k) = J_1 + J_2\cos(k) + \frac{g_0}{2}(1+\cos(5k)), \tag{S22}$$

$$h_y(k) = J_2\sin(k) + \frac{g_0}{2}\mathcal{F}'(k), \tag{S23}$$

where $g_0 = \gamma_0/2$ $(-\gamma_0/2)$ for $d = \lambda_0/4$ $(3\lambda_0/4)$ and $\mathcal{F}'(k) = \sum_{j=1}^{5} 2(-1)^{j-1}\sin(jk) - \sin(5k)$. Therefore, the coherent interaction of the system has the chiral symmetry $\tau_z\mathcal{H}(k)\tau_z = -\mathcal{H}(k)$.

The topology in the auxiliary space $(h_x(k), h_y(k))$ is shown in Fig. S2(b). Topologies in the auxiliary space are distinct for emitter arrays with different sizes. For large arrays, long-range interactions lead to complex topology. Although the topology in quasi-momentum space is changed by varying the size of the system, the hybridization between environment-induced interaction and dimerized interaction only yields shift along k_x axis. Therefore, emitter arrays with different sizes have the same topological phase transition, i.e., at $\gamma_0 = \Delta\omega$, as shown in Fig. S2(c). The energy bands are

$$\varepsilon_\pm(k) = \pm\sqrt{h_x(k)^2 + h_y(k)^2}. \tag{S24}$$

The topological phase transition starts from the gap closing of energy bands. In Fig. S2(c), we present the phase diagram with the open boundary conditions in the dimerized interaction. Namely, for $\gamma_0 = 0$ (the original SSH model) the system is in the topological phase with edge states when $J_1 < J_2$, but in the non-topological phase when $J_1 > J_2$. For the scenario $J_1 < J_2$, i.e., the system is in the topological phase with edge states (TP-I), the environment produces the topological phase transition with the edge-bulk correspondence between TP-I and the non-topological phase (NTP). However, when $J_1 > J_2$, the system changes from the non-topological phase to the topological phase without edge state (TP-II) via a topological phase transition without the edge-bulk correspondence. In this work, we are interested in the topological phase transition with the edge-bulk correspondence, i.e., $J_1 < J_2$. In Fig. S3(a),

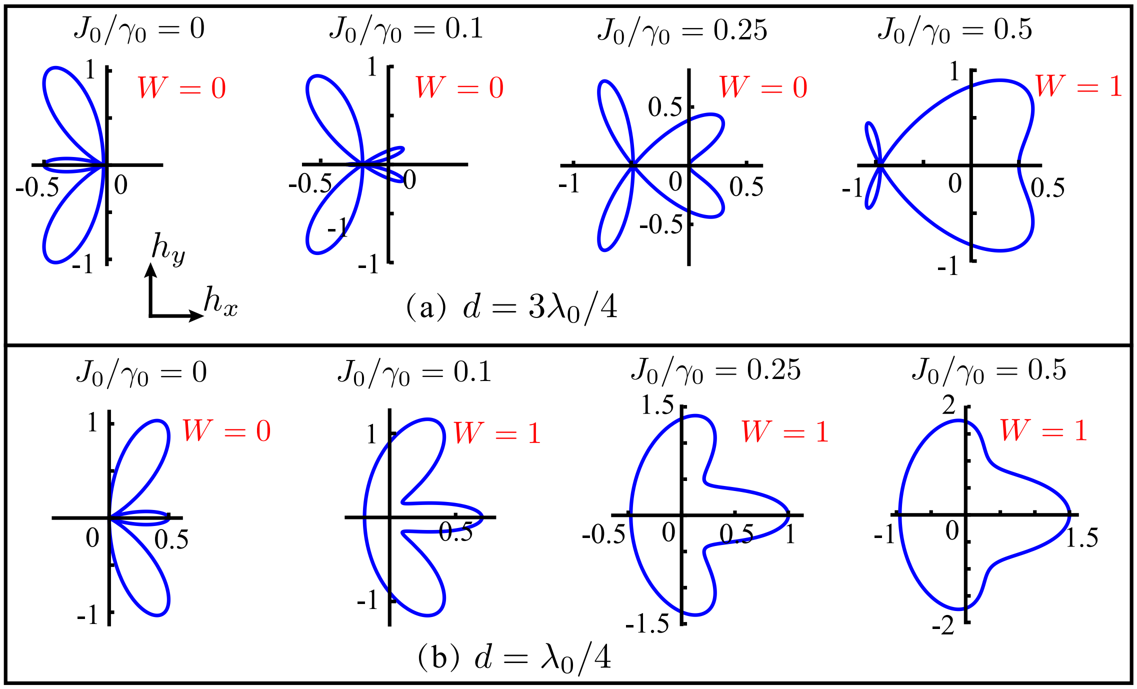

FIG. S3. Topologies from the hybridization between H_{topo} and H_{ph} in auxiliary space $(h_x(k), h_y(k))$ for (a) $d = 3\lambda_0/4$ and (b) $d = \lambda_0/4$. Here, we consider $\varphi = 0.1\pi$ and $N = 6$.

we show the topologies in the auxiliary space for $d = 3\lambda_0/4$. The winding number is zero for $0 \leq J_0 \leq \gamma_0/4$, and becomes one for $J_0 > \gamma_0/4$. Figure S3(b) shows the topologies for $d = \lambda_0/4$. The winding number is zero at $J_0 = 0$, and becomes one for $J_0 > 0$. Therefore, for $d = \lambda_0/4$, the system is topological when $J_0 > 0$. However, the nontrivial topology in the Hamiltonian does not guarantee the stability of the edge states. The stability is determined by the Lindblad operator. Actually, the topological phase for $d = \lambda_0/4$ is not protected by the Lindblad operator.

In Figs. S4(a), S4(b) and S4(c), we show the energy bands for the points A, B and C in Fig. S2(c). Figure S4(a) presents the energy bands in the topological phase of the SSH model. The topological phase transition takes place when the band gap is closed at $k = \pm\pi$, as shown in Fig. S4(b). Without considering the environment, i.e., $g_0 = 0$, the spectrum width of the topological emitter array becomes

$$\begin{aligned} \Delta\omega &= \varepsilon_+(k=0) - \varepsilon_-(k=0), \\ &= 2(J_1 + J_2), \end{aligned} \tag{S25}$$

and the band gap

$$\begin{aligned} \delta\omega &= \varepsilon_+(k=\pi) - \varepsilon_-(k=\pi), \\ &= 2|J_1 - J_2|. \end{aligned} \tag{S26}$$

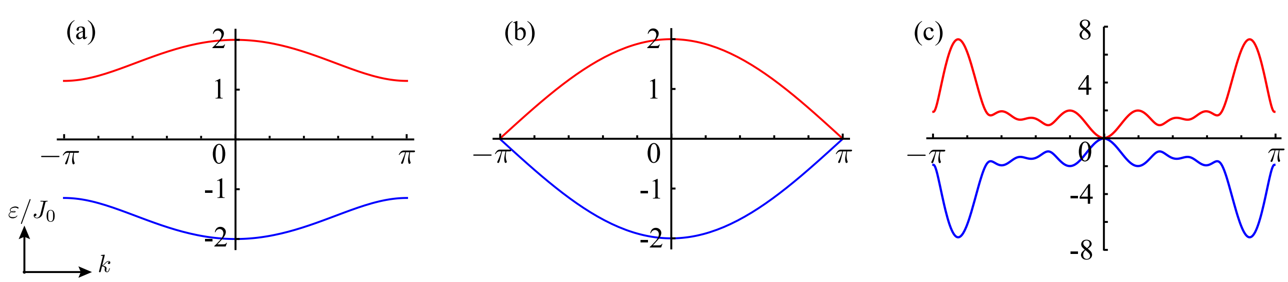

FIG. S4. Band structure for the topological emitter array with (a) $\varphi = 0.3\pi, \gamma_0 = 0$, (b) $\varphi = 0.5\pi, \gamma_0 = 0$, (c) $\varphi = 0.3\pi, \gamma_0 = \Delta\omega$. Here, we consider the array with $N = 10$ emitters.

In the environment, the *dissipation-induced phase transition closes the band gap at* $k = 0$, as shown in Fig. S4(c). From the band gap closing at $k = 0$, we can obtain the *condition for the dissipative topological phase transition*

$$\gamma_0 = 2(J_1 + J_2). \tag{S27}$$

Note that the *different band gap closings* in Fig. S4(b) and Fig. S4(c) with *linear and parabolic dispersions indicate distinct topological criticalities* for the SSH-type topological phase transition and the dissipative topological phase transition [S3].

(II-B) Topological phase transition via perturbation theory: numerical method

In real space, the environment-mediated effective Hamiltonian of the topological emitter array can be written as

$$H = \gamma_0 \tilde{H}_{\mathrm{ph}} + J_0 \tilde{H}_{\mathrm{topo}}, \tag{S28}$$

where $\tilde{H}_{\mathrm{ph}} = H_{\mathrm{ph}}/\gamma_0$ and $\tilde{H}_{\mathrm{topo}} = H_{\mathrm{topo}}/J_0$. At first, we study the noninteracting emitter array, i.e., $J_0 = 0$. We consider $\tilde{H}_{\mathrm{ph}}|\mu_m\rangle = \varepsilon_m|\mu_m\rangle$, where m changes from $-M$ to M, with $M = (N-1)/2$. Here, ε_m denote energy-ordered eigenvalues with $\varepsilon_m \geq \varepsilon_{m-1}$; $|\mu_m\rangle$ are the corresponding eigenvectors.

In Fig. S5(a), the energies ε_m are shown for $N = 5$ (red-dashed) and $N = 7$ (blue-solid). The zero-energy state is found at emitter spacings $d = \lambda_0/4$ and $d = 3\lambda_0/4$. At $J_0/\gamma_0 = 0$, the zero mode in the system is non-topological. For $J_0 \gg \gamma_0$, a topological edge state is obtained.

For values of J_0/γ_0 in between $J_0 = 0$ and $J_0 \gg \gamma_0$, the competition between these two types of interactions leads to an unconventional edge state which has both topological and non-topological features. Here, we are interested in how a topological system with small spectrum width survives in the environment; therefore, J_0 is smaller than or comparable with γ_0 ($J_0 \lesssim \gamma_0$). From Eq. (S28), we obtain

$$H/\gamma_0 = \sum_{m=-M}^{M} \varepsilon_m |\mu_m\rangle\langle\mu_m| + \frac{J_0}{\gamma_0} \sum_{n,m=-M}^{M} \alpha_{nm} |\mu_n\rangle\langle\mu_m|, \tag{S29}$$

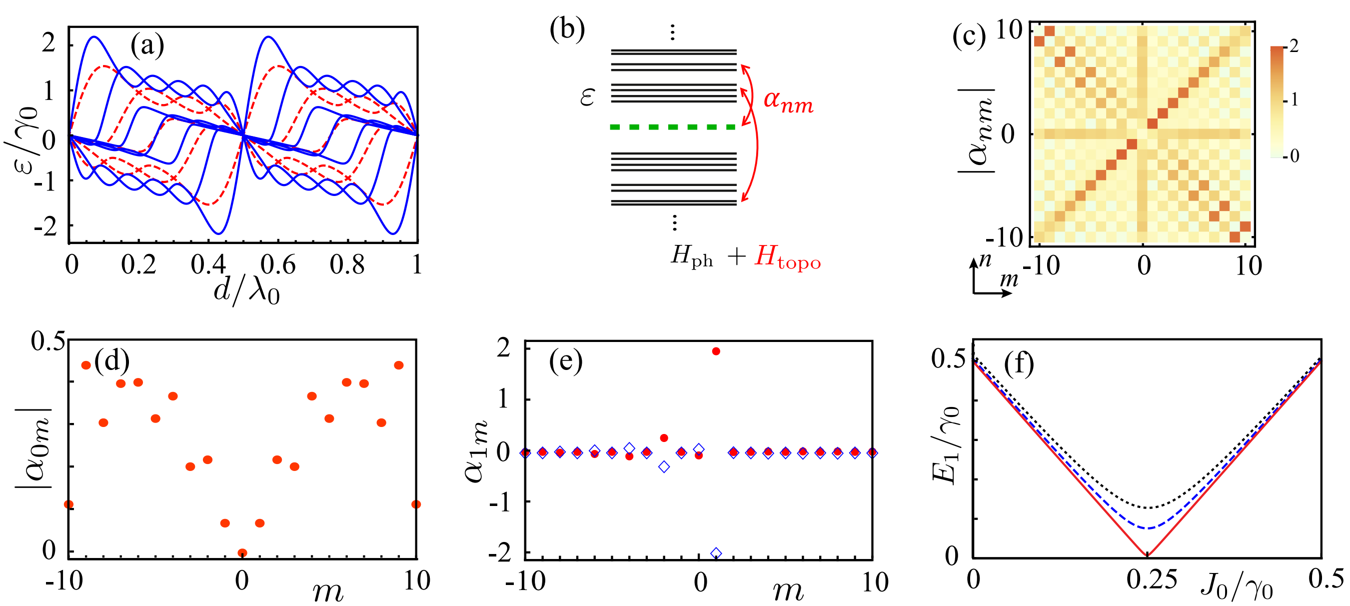

FIG. S5. (a) Energy spectrum of the environment-mediated interactions. (b) The interactions in the topological emitter array produces transitions between different eigenstates of H_{ph}. (c) Absolute values of the elements of the transition matrix α_{nm}. (d) Absolute values of the transition elements between the edge state and the bulk states. (e) Transition elements between the eigenstates of H_{ph} and the bulk state above the edge state. (f) Energy of the bulk state above the edge state for the emitter array with $N = 11$ (black-dotted), $N = 21$ (blue-dashed) and $N = 201$ (red-solid), respectively.

where $\alpha_{nm} = \langle\mu_n|\tilde{H}_{\rm topo}|\mu_m\rangle$ are the transition matrix elements produced by the SSH interaction, as shown in Fig. S5(b). In Fig. S5(c), we show $|\alpha_{nm}|$ for $d = \lambda_0/4$ and $d = 3\lambda_0/4$. From the diagonal components, we know that states close to the zero-energy state are significantly shifted. The off-diagonal components show that the SSH interaction produces couplings between low-energy and high-energy states. The zero-energy state has finite couplings to other states.

For small values of J_0/γ_0, we can obtain the energies of the hybridized eigenstates by perturbation theory,

$$E_m/\gamma_0 = \varepsilon_m + \frac{J_0}{\gamma_0}\alpha_{mm} + \frac{J_0^2}{\gamma_0^2}\sum_{n\neq m}\frac{|\alpha_{nm}|^2}{\varepsilon_m - \varepsilon_n} + O\left(\frac{J_0^3}{\gamma_0^3}\right). \tag{S30}$$

Figure S5(d) shows the norm of the transition matrix elements between the zero-energy mode and the other modes $|\alpha_{0m}|$. It can be seen that $|\alpha_{0m}|$ is symmetric and $\alpha_{00} = 0$. Therefore, E_0/γ_0 is independent of J_0/γ_0. In Fig. S5(e), we show α_{1m} for $d = \lambda_0/4$ and $d = 3\lambda_0/4$. The SSH interaction yields a large energy shift to the state with $m = 1$, but small couplings to other states. In Fig. S5(f), we show the energy E_1 versus J_0/γ_0 for $d = 3\lambda_0/4$. The energy gap between the bulk state and the edge state is closed at $J_0/\gamma_0 = 1/4$ for the system with a large number of emitters.

In the main text, we have studied the energy spectrum from the hybridization between the interactions in the topological emitter array $H_{\rm topo}$ and photon-mediated interactions $H_{\rm ph}$ for systems with an odd number of emitters. A non-topological edge state appears in the topologically trivial phase. It seems that the bulk-edge correspondence is broken, however, it is not.

In Fig. S6, we show the energy spectrum for the system with an even number of emitters. Figure S6(a) plots the spectrum in the regime $|J_0/\gamma_0| \leq 1$. The regimes with $J_0/\gamma_0 < 0$ and $J_0/\gamma_0 > 0$ correspond to the emitter spacing $d = \lambda_0/4$ and $d = 3\lambda_0/4$, respectively. When $J_0 = 0$, only the environment-induced interactions appear. As expected, the system is in the non-topological phase. We now see how the dimerized interactions $H_{\rm topo}$ perturb the environment-induced interactions. With a small portion of negative J_0, the system becomes topological immediately. Interestingly, this topological phase transition takes place *without closing the band gap*. Hence, the energy levels of edge states are separated from each other and they suffer from dissipation. For the positive values of J_0, the band gap is reduced. At the critical value $J_0/\gamma_0 = 1/4$, the bangap is closed, representing a topological phase transition. After the critical point, two degenerate edge states appear and they are dissipationless. Therefore, the topological phases for $d = \lambda_0/4$ and $d = 3\lambda_0/4$ have edge states with different dissipative properties. They correspond to dissipative and dissipationless topological phases, respectively. In Fig. S6(b), we consider the energy spectrum versus γ_0/J_0 in a complementary parameter regime of Fig. S6(a). We find that the environment nontrivially affects energies of the edge states for $d = \lambda_0/4$ and $d = 3\lambda_0/4$. The edge states for $d = \lambda_0/4$ are rapidly separated from each other when $|\gamma_0/J_0|$ increases. However, the edge states for $d = 3\lambda_0/4$ have a small splitting for $\gamma_0/J_0 \ll 1$. They become degenerate when γ_0/J_0 further increases until the DTPT at $\gamma_0/J_0 = 4$ (see Fig. S6(a)).

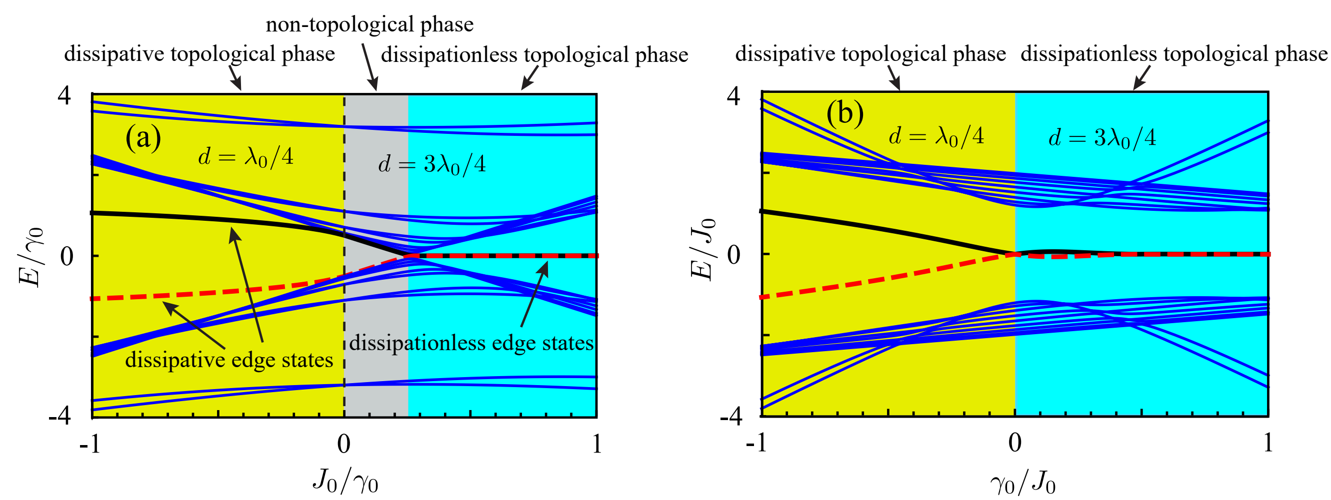

FIG. S6. Energy spectrum from the hybridization between $H_{\rm topo}$ and $H_{\rm ph}$ in the array with an even number of emitters versus (a) J_0/γ_0 and (b) γ_0/J_0. Two topological phase transitions are shown in (a): one is the topological phase transition without closing the band gap at $J_0/\gamma = 0$, the other one is the DTPT closing the band gap at $J_0/\gamma_0 = 1/4$. Here, we consider $\varphi = 0.3\pi, N = 20$.

(III) TOPOLOGICAL PROTECTION: HAMILTONIAN VERSUS LINDBLAD OPERATOR

We have studied the topology in the Hamiltonian. The hybridization between the dimerized interactions and photon-mediated interactions gives rise to topological phase transitions. Can the chiral symmetry in the Hamiltonian protect edge states from dissipation? In the following, we pinpoint the roles played by the Hamiltonian and Lindblad operator in protecting the edge states from dissipation.

(III-A) Hybridization in the Hamiltonian and its consequence in dissipative/dissipationless topological phase

Also, it is helpful to understand how the environment affects the topological emitter array and dissipative property of edge states by considering small values of γ_0. In Fig. S7(a), we show the energy spectrum versus γ_0 for the system with $N = 21$, i.e., a single edge state. From the energy spectrum, the edge state couples to a few bulk states which show anti-crossings at $\gamma_0 = 0$, even though the energy level of the edge state is not shifted. The reason for the unshifted edge state can be understood from perturbation theory, similar to Eq. (S30), i.e., the first perturbation is vanishing, the second perturbations are symmetric.

In Fig. S7(b), we present $|\Gamma_{00}/\gamma_0|$ versus γ_0. We can find that γ_0 changes $|\Gamma_{00}/\gamma_0|$ in different ways for $d = \lambda_0/4$ and $d = 3\lambda_0/4$: $|\Gamma_{00}/\gamma_0|$ quickly reduces to zero for $d = 3\lambda_0/4$, however, it increases rapidly for $d = \lambda_0/4$. *This sudden change of the scaled decay rate $|\Gamma_{00}/\gamma_0|$ of the edge state shows distinct dissipative features of these two topological phases.* Hence, the decay rate Γ_{00} is large in the dissipative topological phase, and reduces to zero in the dissipationless topological phase. For the weak coupling $0 < \gamma_0 \ll 1$, the edge state has low decay rate. In Fig. S7(c), we present $|\Gamma_{00}/\gamma_0|$ and Γ_{00} for a broad range of γ_0. In the regime $\gamma_0 < 0$, i.e., $d = \lambda_0/4$, the decay rate Γ_{00} from the edge state to environment becomes larger with increasing $|\gamma_0|$. However, it becomes zero for $0 < \gamma_0 < 4J_0$, i.e., $d = 3\lambda_0/4$. Therefore, the topological phases for $d = \lambda_0/4$ and $d = 3\lambda_0/4$ are dissipative and dissipationless, respectively.

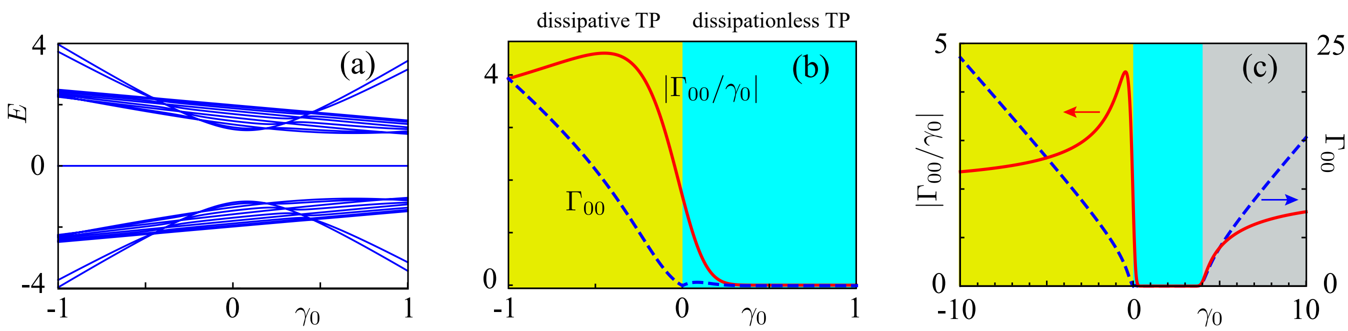

FIG. S7. (a) Energy structure of the Hamiltonian $H_{\mathrm{topo}} + H_{\mathrm{ph}}$. The parameter regimes $\gamma_0 < 0$ and $\gamma_0 > 0$ correspond to $d = \lambda_0/4$ and $d = 3\lambda_0/4$, respectively. (b) The scaled decay rate $|\Gamma_{00}/\gamma_0|$ (red-solid) and decay rate Γ_{00} (blue-dashed) versus γ_0. (c) Changes of $|\Gamma_{00}/\gamma_0|$ and Γ_{00} in a large regime of γ_0. Note that for increasing γ_0 from -10, $|\Gamma_{00}/\gamma_0|$ increases slowly, and suddenly drops down. And then it keeps zero and increases near the critical point. Here, we consider $J_0 = 1, \varphi = 0.3\pi, N = 21$.

(III-B) Dissipationless edge states in finite systems

The environment-induced long-range interactions greatly modify the edge states (see Figs. S7(a) and S7(b)). In the original SSH model, the edge states are exponentially localized on the odd- and even-site emitters, depending on the parameter φ. For example, the left-localized edge state is

$$\begin{aligned} |\psi_0\rangle_L &= \frac{1}{\sqrt{\mathcal{N}}} \sum_n \left(-\frac{J_1}{J_2}\right)^{n-1} |A\rangle_n, \\ &= \frac{1}{\sqrt{\mathcal{N}}} \sum_n (-1)^{n-1} \left(\tan\frac{\varphi}{2}\right)^{2n-2} |A\rangle_n, \end{aligned} \tag{S31}$$

where n denotes the nth unit cell of the emitter array and $|A\rangle_n = \sigma^+_{A,n}|G\rangle$. Here, $\mathcal{N}$ is a normalization factor. The polarizations of edge states are protected by the chiral symmetry of the system. In our model, the long-range

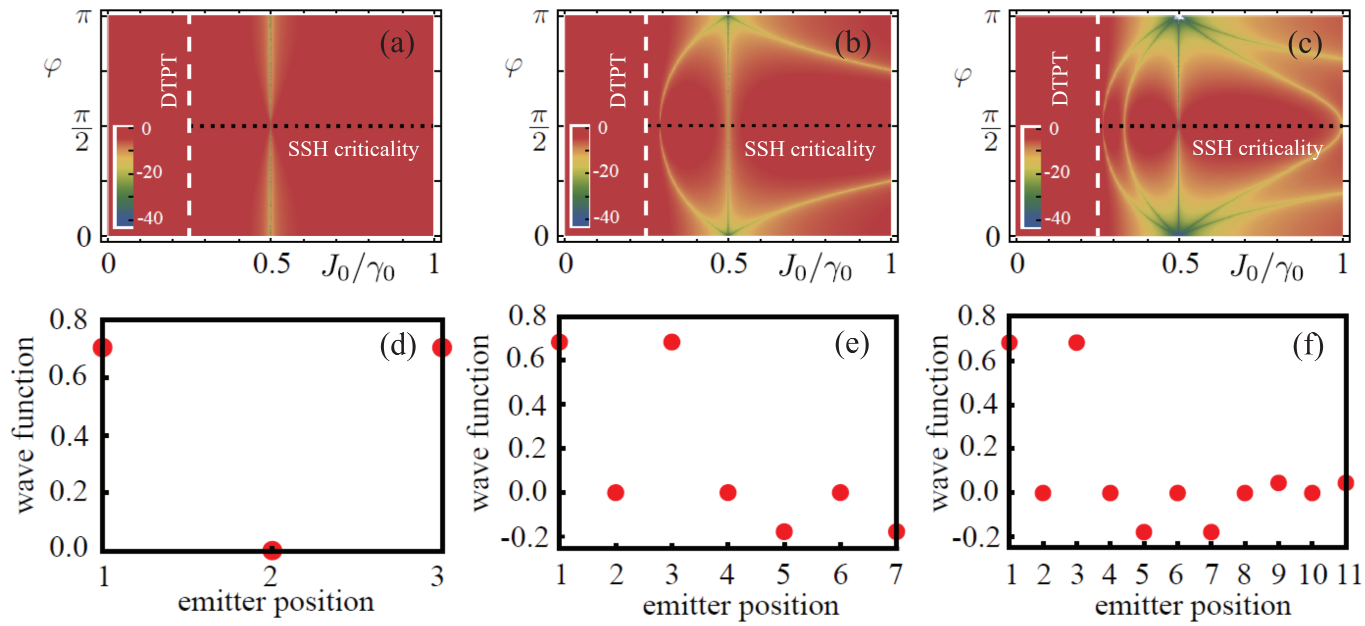

FIG. S8. Logarithm of the scaled decay rate of the edge state $\ln(\Gamma_{00}/\gamma_0)$ for emitter arrays with (a) $N=3$, (b) $N=7$ and (c) $N=11$. Wave function of edge state for topological emitter arrays with (d) $N=3$, (e) $N=7$, (f) $N=11$; and $J_0/\gamma_0=0.5, \varphi=0.3\pi$. The black-dotted and white-dashed lines denote the SSH criticality and DTPT, respectively. Here, we consider emitter spacing $d=3\lambda_0/4$.

interactions induced by the environment preserve the chiral symmetry $\tau_z\mathcal{H}(k)\tau_z=-\mathcal{H}(k)$. Therefore, the polarization of the edge states are protected. However, the interplay between the long-range interactions and dimerized interactions leads to various forms of edge states. Namely, the concrete forms of edge states depend on the parameters J_0/γ_0 and φ. By considering the Lindblad operator, we can study dissipation properties of the edge states. In Figs. S8(a)-S8(c), we show the dissipative property of edge states in small systems with $N=3,7$ and 11, respectively. The minimum of $\ln(\Gamma_{00}/\gamma_0)$ represents the parameter space where the edge state becomes dissipationless. The white-dashed and black-dotted lines denote the DTPT and the SSH criticality, respectively.

In particular, when the environment-induced decay rate γ_0 is half of the spectrum width $\Delta\omega$, the edge states have the same amplitudes at the $(4i+1)$th and the $(4i+3)$th emitters, different from the original SSH model. For the minimal system with $N=3$ emitters, shown in Fig. S8(a), the edge state at $J_0/\gamma_0=0.5$ is the equal superposition between the first and third emitters as shown in Fig. S8(d). In Fig. S8(e), we present the wave function of the edge state at $J_0/\gamma_0=0.5$ and $\varphi=0.3\pi$ for the emitter array with $N=7$. The *exponentially localized dissipationless edge state is*

$$\left|\psi_0\left(\frac{J_0}{\gamma_0}\to\frac{1}{2}\right)\right\rangle=\frac{1}{\sqrt{\mathcal{N}}}\sum_{n=0}^{M}(-1)^n\left(\tan\frac{\varphi}{2}\right)^{2n}|\psi\rangle_n, \tag{S32}$$

with $M=\text{Quotient}[N,4]$ and $|\psi\rangle_n=(\sigma^+_{4n+1}+\sigma^+_{4n+3})|G\rangle$. The $(4n+1)$th and $(4n+3)$th emitters have the same amplitude. The edge state for $N=11$ with $J_0/\gamma_0=0.5$ and $\varphi=0.3\pi$ is shown in Fig. S8(f).

The local minima of $\ln(\Gamma_{00}/\gamma_0)$ demonstrates the dark edge state. It can be seen from Figs. S8(a), S8(b) and S8(c) that more dark edge states can be found in the topological phase for larger systems.

Figure S9(a) shows $\ln(\Gamma_{00}/\gamma_0)$ versus γ_0/J_0 and φ for the emitter array with $N=15$. In the topological phase, the edge state has much lower dissipation than in the non-topological phase. As the system gets close to the SSH criticality (black-dotted line), the edge state becomes more dissipative, except for some trajectories characterized by the minima of $\ln(\Gamma_{00}/\gamma_0)$. In the system with an odd number of emitters, there is a single edge state. This edge state is localized to the left boundary if the value of $\varphi\in[0,\pi/2)$, and localizes to the right boundary for $\varphi\in(\pi/2,\pi]$. In Fig. S9(b), we study the dissipation property of edge states for the emitter array $N=20$. In arrays with an even number of emitters, non-topological phase is found in parameter regimes 1) $\pi/2<\varphi\leq\pi$ and $\gamma_0/J_0<4$, 2) $0\leq\varphi<\pi/2$ and $\gamma_0/J_0>4$. The topological phase without edge state (TP-II) is found in the regime $\pi/2<\varphi\leq\pi$ and $\gamma_0/J_0>4$. These parameter regimes imply the protection of the topological edge states by the Lindblad operator.

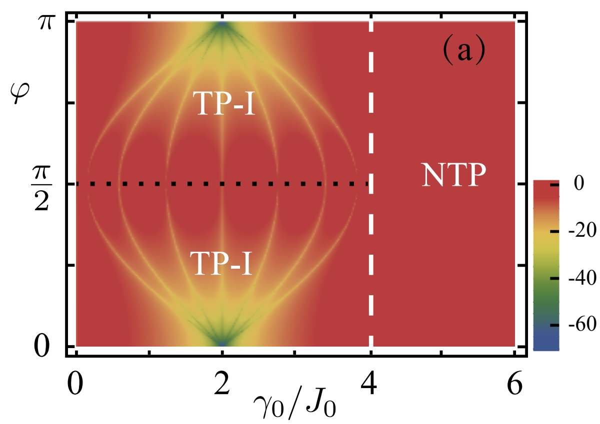

FIG. S9. Logarithm of the scaled decay rate $\ln(\Gamma_{00}/J_0)$ of the edge state (in the topological phase TP-I) for emitter arrays with (a) $N = 15$ and (b) $N = 20$. The black-dotted and white-dashed lines denote the SSH criticality and DTPT, respectively. The white-solid line is the topological phase transition between the non-topological phase (NTP) and the topological phase without edge state (TP-II).

(III-C) Dissipation spectrum: how the Lindblad operator protects dissipationless edge states

To further understand the dissipative properties of topological phases, we study the Lindblad operator

$$\mathcal{D}[\rho] = \sum_{i,j=1}^{N} \gamma_{ij}(\sigma_i^- \rho \sigma_j^+ - \frac{1}{2}\sigma_i^+ \sigma_j^- \rho - \frac{1}{2}\rho \sigma_i^+ \sigma_j^-). \tag{S33}$$

We consider the dissipative matrix γ with matrix elements γ_{ij} in the Lindblad operator. For the emitter spacings $d = \lambda_0/4$ and $d = 3\lambda_0/4$, the systems have the same dissipative matrix γ, as shown in Fig. S10. Interestingly, the dissipation exhibits the parity property, i.e., the odd-site (even-site) emitters only dissipate to odd-site (even-site) emitters. Owing to the parity in the Lindblad operator, the variations of edge states in the Hamiltonian for $d = \lambda_0/4$ and $d = 3\lambda_0/4$ will yield distinct dissipative properties. To study this, we diagonalize the dissipative matrix

$$\gamma = \sum_m \chi_m |\chi_m\rangle\langle\chi_m|. \tag{S34}$$

The dissipation spectrum χ_m is shown in Fig. S11(a). We find that there are two radiating modes with large decay rates. Their wave functions are shown in Figs. S11(b) and S11(c). They correspond to polarized states of even- and odd-site emitters, respectively. Note that in the system with odd number of emitters, the odd-site polarized radiating mode has larger decay rate than the even-site polarized mode. The decay rate Γ_{00} from the edge state to environment

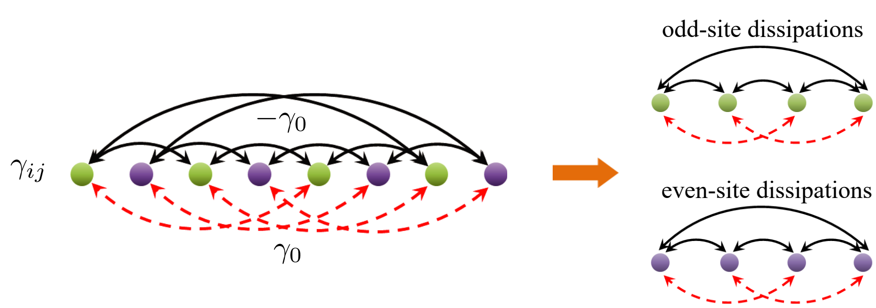

FIG. S10. Environment-induced dissipations between emitters for $d = \lambda_0/4$ and $d = 3\lambda_0/4$ in the Lindblad operator. The dissipation has the parity property: odd-site (even-site) emitters only dissipate to odd-site (even-site) emitters.

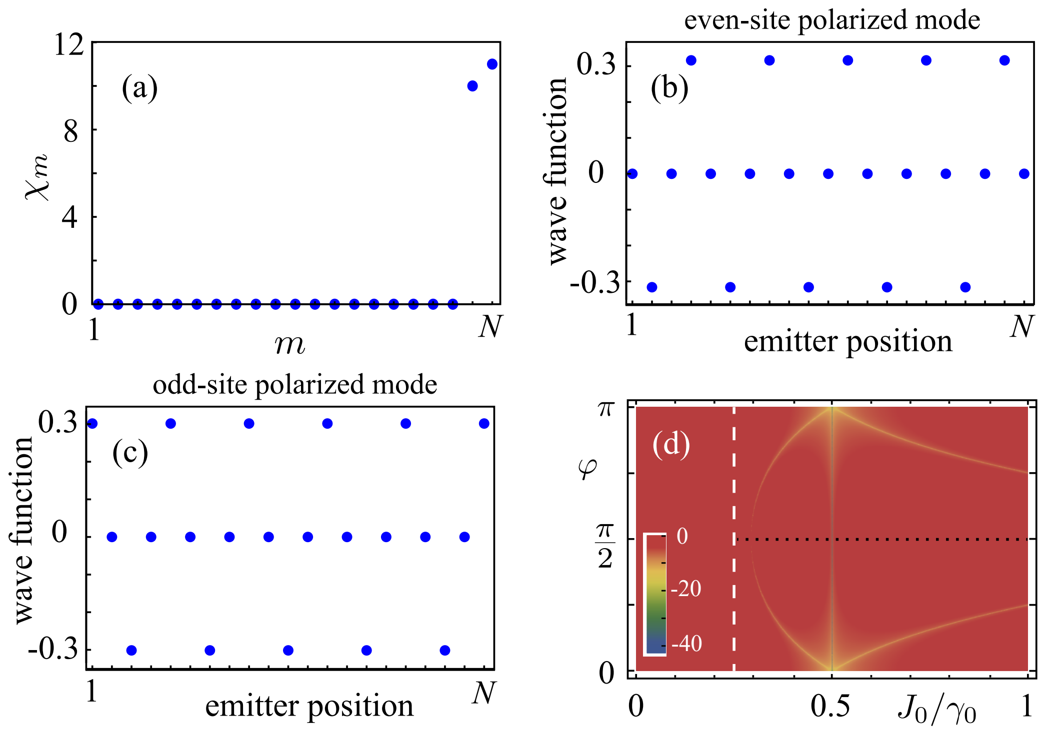

FIG. S11. (a) Dissipation spectrum. Two modes are found to be radiating. (b) The radiating mode $|\chi_{N-1}\rangle$ has even-site polarization. (c) The other radiating mode $|\chi_N\rangle$ has odd-site polarization. (d) Logarithm of the overlap $\langle\Psi_0|\chi_N\rangle$ between the edge state $|\Psi_0\rangle$ and the radiating mode $|\chi_N\rangle$. Here, we consider $N = 21$ in (a,b,c) and $N = 7$ in (d).

can be rewritten as

$$\begin{aligned}\Gamma_{00} &= \langle\Psi_0|\gamma|\Psi_0\rangle \\ &= \sum_m \chi_m \langle\Psi_0|\chi_m\rangle^2.\end{aligned} \tag{S35}$$

Namely, the decay rate Γ_{00} is controlled by the overlap between the edge state and radiating modes in the Lindblad operator. Similarly, the decay rate between the edge state and the nth bulk state is

$$\Gamma_{n0} = \sum_m \chi_m \langle\Psi_0|\chi_m\rangle\langle\chi_m|\Psi_n\rangle. \tag{S36}$$

Therefore, the dissipative properties of edge states are determined by how they overlap with these two radiating modes. In other words, the dissipationless edge state is obtained by $\langle\Psi_0|\chi_m\rangle \approx 0$ for $m = N-1$ and N. Owing to the chiral symmetry, the edge states are polarized with the odd- or even-site emitters.

In the system with odd number of emitters, there is a single edge state polarized with odd-site emitters. So, the parameter space for dissipationless edge state is determined by the condition that the edge state has vanishing overlap with the odd-site polarized mode, i.e., $\langle\Psi_0|\chi_N\rangle \approx 0$, as shown in Fig. S11(d). The parameter space is as same as the one in Fig. (S8)(b). Therefore, *the chiral symmetry in the photon-mediated interaction not only plays an important role in determining the topology of the Hamiltonian, but also yields the parity property in the Lindblad operator.* The interplay between edge states and polarized radiating modes in the Lindblad operator gives rise to the parameter space protecting edge states from dissipation. When the topological emitter array is large enough, the parameter space for dissipationless edge states spans the whole topological phase.

(III-D) Robustness of dissipationless edge states

In Fig. S12(a), we present the energy structure of the Hamiltonian $H = H_{\rm topo} + H_{\rm ph}$. The Lindblad operator is responsible for the decay of the edge state excitation, including the dissipation Γ_{00} from the edge state to the

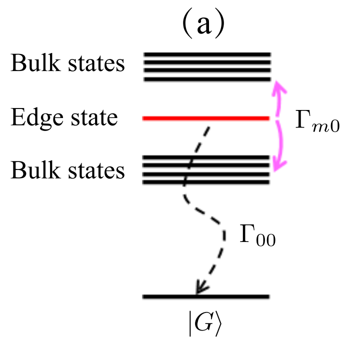

FIG. S12. (a) Environment-induced dissipations of the topological emitter array. Here, Γ_{00} denotes radiation from the edge state to the environment, Γ_{m0} is the radiation from the edge state to the mth bulk state. (b) Effective model by taking into account the dissipative coupling in the Lindblad operator.

environment and the dissipations Γ_{m0} from the edge state to bulk states. Here, the edge-bulk dissipations are reciprocal: $\Gamma_{m0} = \Gamma_{0m}$. In the main text, we show that the edge states can be dissipationless for the emitter spacing $d = 3\lambda_0/4$ due to the protection of chiral symmetry. However, when the emitter spacing deviates from $3\lambda_0/4$, the chiral symmetry might be broken.

To investigate if the dissipationless edge states are robust to disorder in the emitter spacing, we study the decay rate Γ_{00} from the edge state to the environment in Fig. S13(a). Surprisingly, Γ_{00} is low for the emitter spacings around $3\lambda_0/4$ when γ_0/J_0 is changed. A window for low-decaying edge state emerges. We also consider the largest decay rate $\Gamma_{m'0}$ from the edge state to bulk states in Fig. S13(b). A similar window is found around $3\lambda_0/4$ for the edge-bulk dissipation. Because of the dissipationless window, we can expect that the dissipationless edge state is robust to the variation in the emitter spacing.

To further confirm the existence of the dissipationless window, we describe the whole system with a non-Hermitian effective Hamiltonian

$$H_{\text{eff}} = H_{\text{topo}} + H_{\text{ph}} + H'_{\text{ph}}, \tag{S37}$$

where H'_{ph} denotes the environment-induced dissipative (non-Hermitian) coupling contained in the Lindblad operator. The non-Hermitian effective Hamiltonian can be written as a diagonalized form

$$H_{\text{eff}} = \sum_j (\tilde{E}_j - i\tilde{\Gamma}_j)|\tilde{\Psi}_j^R\rangle\langle\tilde{\Psi}_j^L|, \tag{S38}$$

where $|\tilde{\Psi}_j^R\rangle$ and $\langle\tilde{\Psi}_j^L|$ are the right and left eigenvectors, and they form the biorthogonal basis with $\langle\tilde{\Psi}_j^L|\tilde{\Psi}_{j'}^R\rangle = \delta_{jj'}$. We can obtain the effective decay rate $\tilde{\Gamma}_{j_0}$ of the edge state, as schematically shown in Fig. S12(b). We find that there is indeed a dissipationless window around $d = 3\lambda_0/4$ for various values of γ_0/J_0, as shown in Fig. S14(a). Interestingly,

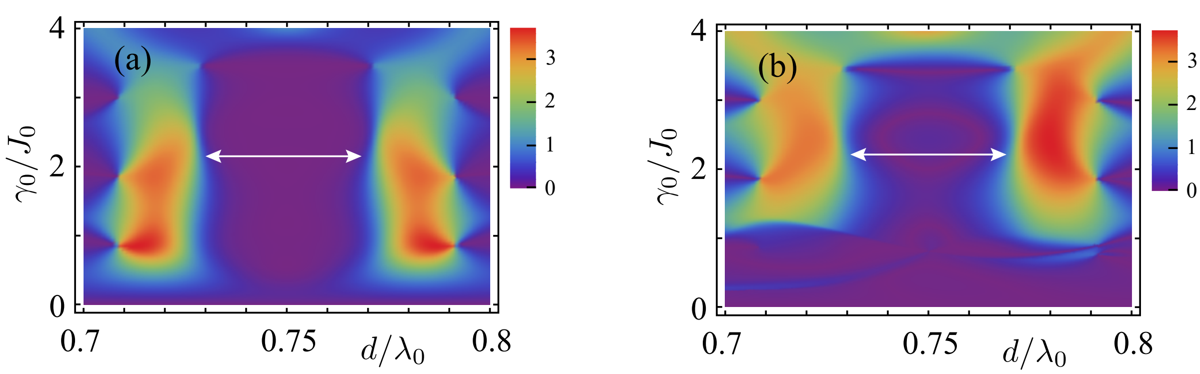

FIG. S13. (a) Decay rate Γ_{00} from the edge state to the environment. (b) Absolute value of the largest decay rate $|\Gamma_{m'0}|$ from the edge state to bulk states. Here, we consider $N = 11, \varphi = 0.3\pi$.

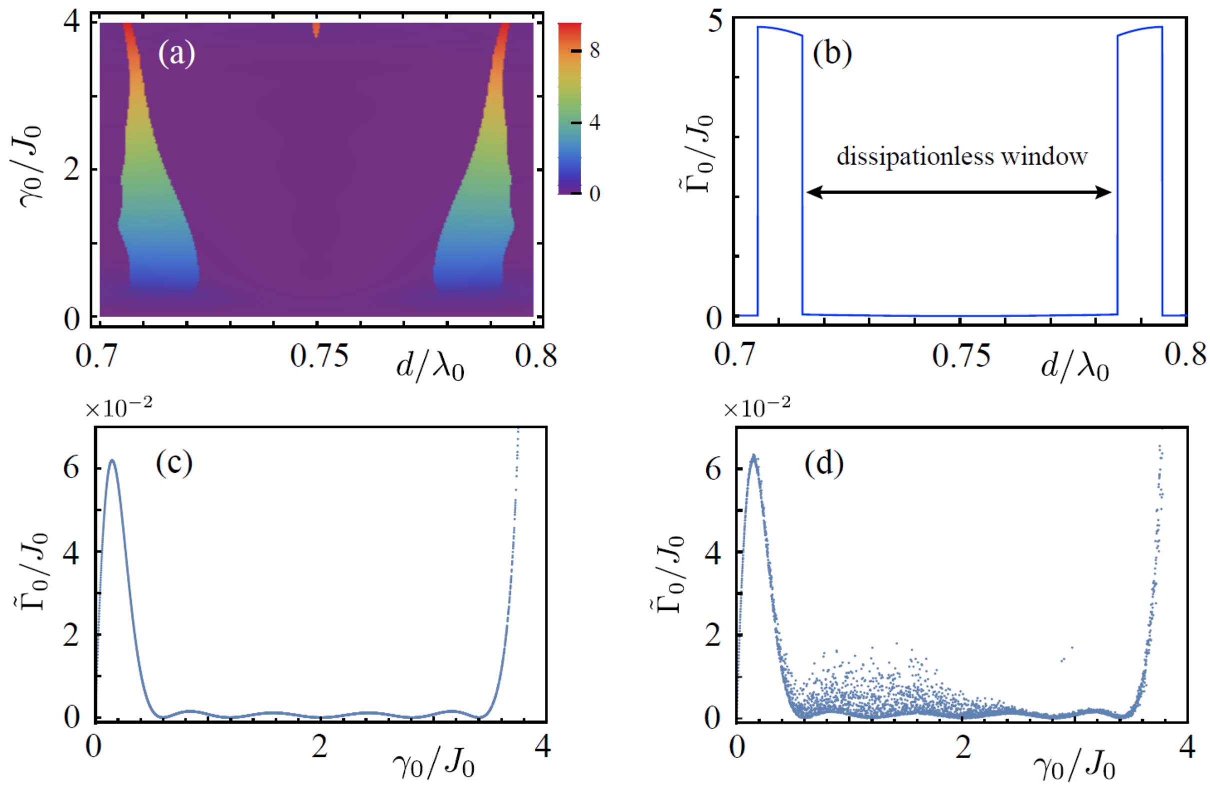

FIG. S14. (a) Logarithm of the scaled decay rate $\tilde{\Gamma}_{j_0}/J_0$ of the edge state for various values of d/λ_0 and γ_0/J_0. A dissipationless window for the edge state exists for various values of γ_0 in the topological phase, except for weak system-environment coupling, $\gamma_0 \ll J_0$. (b) Scaled decay rate $\tilde{\Gamma}_{j_0}/J_0$ of the edge state for $\gamma_0 = 2J_0$. The dissipationless window is about $0.07\lambda_0$. (c) $\tilde{\Gamma}_{j_0}/J_0$ versus γ_0/J_0 for the disorder strength $\varsigma \in [-0.002, 0.002]$. (d) $\tilde{\Gamma}_{j_0}/J_0$ affected by the strong disorder $\varsigma \in [-0.02, 0.02]$. The parameters are: $N = 11, \varphi = 0.3\pi$.

the dissipationless window becomes wider when γ_0/J_0 is increased. This means that the strong system-environment coupling makes the edge state more robust. When $\gamma_0 \ll J_0$, the edge state becomes dissipative and the window disappears. In Fig. S14(b), we show the effective decay rate of the edge state at $\gamma_0/J_0 = 2$. The dissipationless window width becomes $\Delta d \approx 0.07\lambda_0$. This actually provides a large range of parameter space to tolerate disorder in the emitter spacing.

The dissipationless window provides a protection to disorder in the emitter spacing. It guarantees the feasibility for the experimental observation of dissipationless edge states. The electromagnetic-controlled topological emitter array can be implemented in superconducting quantum circuits where the interaction between emitters and the coupling between emitters and 1D continuous photonic modes have been realized.

The electromagnetic environment can be realized with a one-dimensional waveguide. Without loss of generality, we assume that the frequency of superconducting artificial atoms $\omega_0/2\pi \sim 5$GHz. Therefore, the wavelength λ_0 of the photons with that frequency in the waveguide is about 0.06 m. The typical size of the superconducting artificial atom is $\sim 100\ \mu$m. We assume that the position of the ith atom is $x_i = (i-1)d + \varsigma\lambda_0$, where ς is the disorder parameter. In Fig. S14(c), we consider the disorder of emitter positions $\varsigma \in [-0.002, 0.002]$, i.e., the disorder strength is about the size of superconducting artificial atom. The decay rate of the edge state is almost not affected. In Fig. S14(d), we consider the strong disorder $\varsigma \in [-0.02, 0.02]$, i.e., the disorder strength is about 10 times the size of superconducting artificial atom. The dissipation of the edge state is not sensitive to the strong disorder in the weak coupling regime for the reason that there is no window. When γ_0/J_0 is increased, the effective decay rate of the edge state becomes larger for two reasons: 1) the dissipationless window is narrow, 2) the decay rates are large near the window boundaries (see Fig. S14(b)). As γ_0/J_0 further increases, the disorder becomes not important because the dissipationless window is large enough (see Fig. S14(a)). For the potential experimental realization (scenario of Fig. S14(c)), the dissipationless edge state can be observed.

We also consider the effective decay rate for the emitter spacing $d = \lambda_0/4$ in Fig. S15(a). Compared with the edge state at $d = 3\lambda_0/4$, the dissipation is significantly changed when the emitter spacing varies around $d = \lambda_0/4$. In

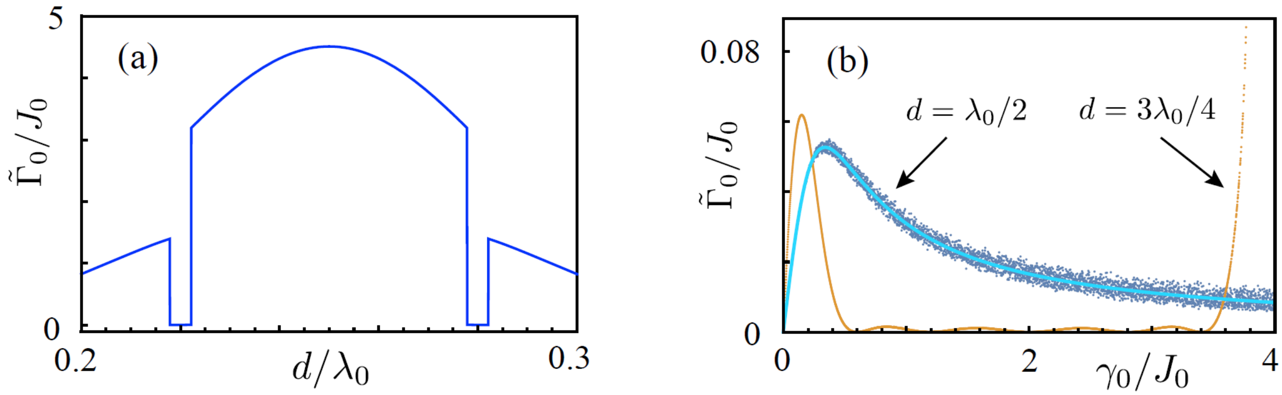

FIG. S15. (a) Effective decay rate of the edge state for the emitter spacing $d = \lambda_0/4$. (b) Effective decay rate of the edge state for the emitter spacings $d = \lambda_0/2$ and $d = 3\lambda_0/4$, for the disorder strength $\varsigma \in [-0.002, 0.002]$ of the emitter spacing. The light blue curve is the effective decay rate for $d = \lambda_0/2$ without considering the disorder. Here, we assume $\varphi = 0.3\pi, N = 11$.

this work, we focus on the study of emitter spacings $d = \lambda_0/4$ and $d = 3\lambda_0/4$. Actually, for the emitter spacings $d = n\lambda_0/2$ ($n = 0, 1, 2, \cdots$), the photon-mediated interactions are zero. Therefore, the chiral symmetry is also preserved. However, the Lindblad operator does not protect the edge state from dissipation, as shown in Fig. S15(b). Compared with $d = 3\lambda_0/4$, the effective decay rate of the edge state for $d = \lambda_0/2$ is more sensitive to the disorder in emitter spacing. This indicates important roles of the photon-mediated interactions and the interplay between the Hamiltonian and Lindblad operator. The dissipationless window for $d = 3\lambda_0/4$ provides a practical protection for observing dissipationless edge states in experiments.

The dissipationless window for $d = 3\lambda_0/4$ shows the robustness of edge states to the disorder in long-range interactions. It is interesting to ask if the dissipationless window provides a protection for edge states from the disorder of dimerized interaction. We consider the dimerized interaction with disorder $J_{1,2} + \xi J_0$, where ξ is the disorder parameter. We study the effect of disorder in dimerized interaction with the disorder strength $\xi \in [-0.1, 0.1]$ in Fig. S16(a) and $\xi \in [-0.3, 0.3]$ in Fig. S16(b). Different from the disorder in emitter spacing as we studied in Fig. S14(d), the dissipationless window does not protect the edge states from the disorder in the dimerized interaction. In other words, as the window is increased for large γ_0/J_0 (see Fig. S14(a)), the effect of disorder is not suppressed. However, the edge states are protected from dissipation when disorder in the dimerized interaction is introduced. This is because in the topological phase, the dissipation of the edge state is not sensitive to the change of J_0 (see Fig. 4(a) in the main text).

In the main text, we have shown that the strong coupling leads to the degeneracy of edge states. The edge-state degeneracy is protected by the chiral symmetry in the emitter spacing $d = 3\lambda_0/4$. If the chiral symmetry is broken, the degeneracy might be shifted. In Fig. S17(a), we show the energy splitting between edges states versus the emitter spacing. The degeneracy between edge states is not guaranteed for general emitter spacings. However,

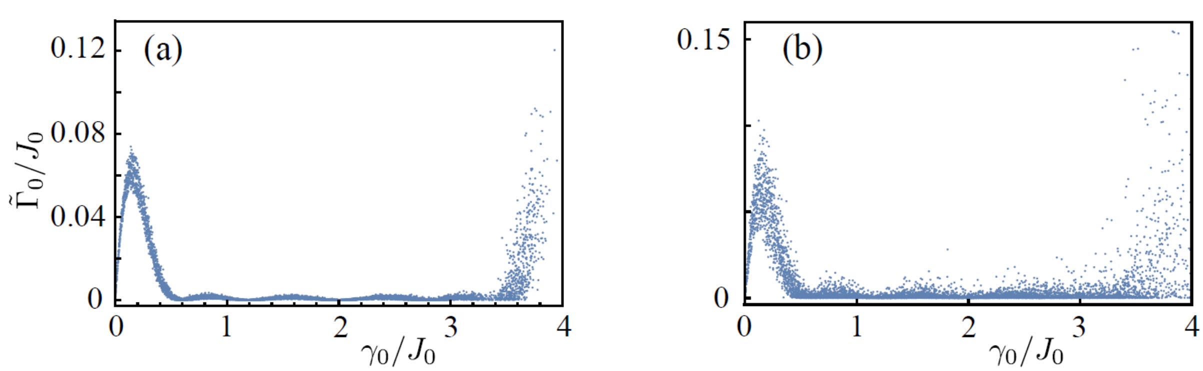

FIG. S16. Effect of disorder in the dimerized interaction $J_i + \xi J_0$, with ξ being the disorder parameter. The disorder parameter is (a) $\xi \in [-0.1, 0.1]$ and (b) $\xi \in [-0.3, 0.3]$. We consider $N = 11, \varphi = 0.3\pi$.

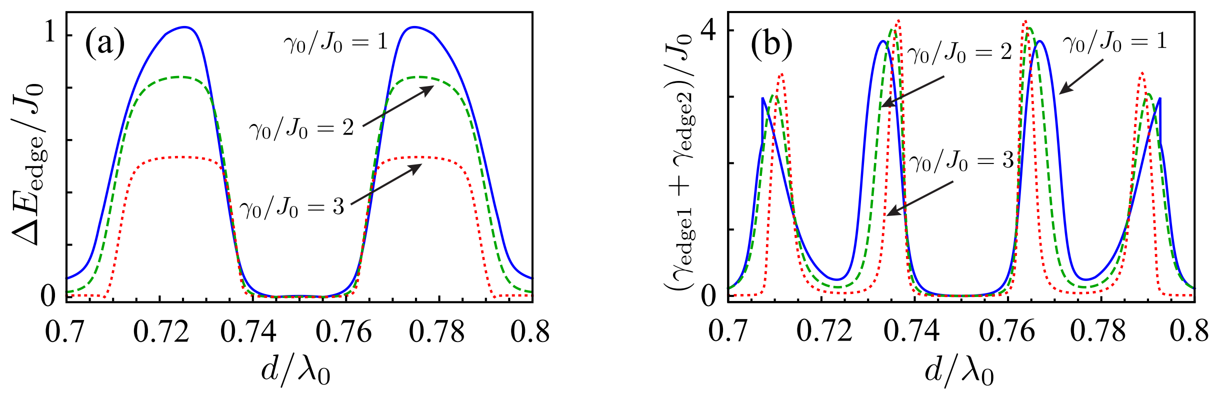

FIG. S17. (a) Energy splitting between edge states. (b) The total dissipation from the subspace of edge states to the environment. We consider $N = 20, \varphi = 0.3\pi$.

around the emitter spacing $d = 3\lambda_0/4$, the degeneracy is still preserved. The energy degeneracy makes the edge states dissipationless. In Fig. S17(b), we present the total dissipation from the subspace of edge states to the environment. The subspace is dissipationless when the edge states are degenerate around $d = 3\lambda_0/4$.

In experiments, emitters can have disorder in their frequencies. In superconducting quantum circuits, frequencies of superconducting artificial atoms can be well-controlled. The disorder in emitter frequency is equivalent to disorder in emitter position. For example, in the experiment by Wen *et al.* [S4], the relative frequency difference between two qubits is $(\omega_2 - \omega_1)/\omega_1 \approx 7.98 \times 10^{-4}$ with qubit frequencies $\omega_1 = 5.01 \times 2\pi$ GHz and $\omega_2 = 5.014 \times 2\pi$ GHz. Therefore, the wavelengths for photons with frequencies ω_1 and ω_2 are $\lambda_1 = 2\pi c/\omega_1 = 59.88$ mm and $\lambda_2 = 2\pi c/\omega_2 = 59.83$ mm. The relative difference between λ_1 and λ_2 is $(\lambda_1 - \lambda_2)/\lambda_1 \approx 8.4 \times 10^{-4}$. For the emitter spacing $d = 3\lambda_0/4$ (with $\lambda_0 = \lambda_1$), the disorder in emitter frequency is equivalent to disorder in emitter position $\sim 1.12 \times 10^{-3}d$. The edge states in the topological system with such disorder are protected by the dissipationless window (see Fig. S15(b)).

(IV) EXPERIMENTAL POSSIBILITY TO OBSERVE THE DISSIPATIVE TOPOLOGICAL PHASE TRANSITION (DTPT)

This work shows the potential for electromagnetic manipulation of topological quantum matter with vacuum fields. Our proposal can be realized in many quantum systems. In the following, we discuss the experimental feasibility for superconducting quantum circuits.

(IV-A) Simulation of the dissipative topological emitter array with superconducting qubits

The dissipative topological phase transition and dissipationless edge states can be realized in present experimental setups. For example, in superconducting quantum circuits, which are currently used for quantum computation and quantum simulation, the qubits have been coupled to 1D electromagnetic environments [S4, S5]. Without loss of generality, we assume that the frequency of qubits is about $\omega_0/2\pi \sim 5$ GHz in superconducting quantum circuits [S4, S5]. The environment-induced decay rate $\gamma_0/2\pi$ has been realized with ~ 100 MHz [S5]. Namely, the photon-qubit coupling $g/2\pi = \sqrt{\gamma_0 c}/2\pi \approx 69.1$ MHz and is much weaker than the single qubit frequency $\omega_0/2\pi \sim 5$ GHz. Hence, the Born-Markov approximation is guaranteed.

The interaction $J_{AB}/2\pi$ between two qubits A and B can be changed via the tunable coupler, e.g., from 0 to 55 MHz [S6]. Hence, the maximum value of $J_0/2\pi$ is about 27.5 MHz because we consider a dimerized interaction of the form $J_i = J_0[1 + (-1)^i \cos\varphi]$. Therefore, the parameter regime for observing the DTPT can be realized by changing J_0. The regime for larger γ_0/J_0 can be realizable by consider smaller values of J_0.

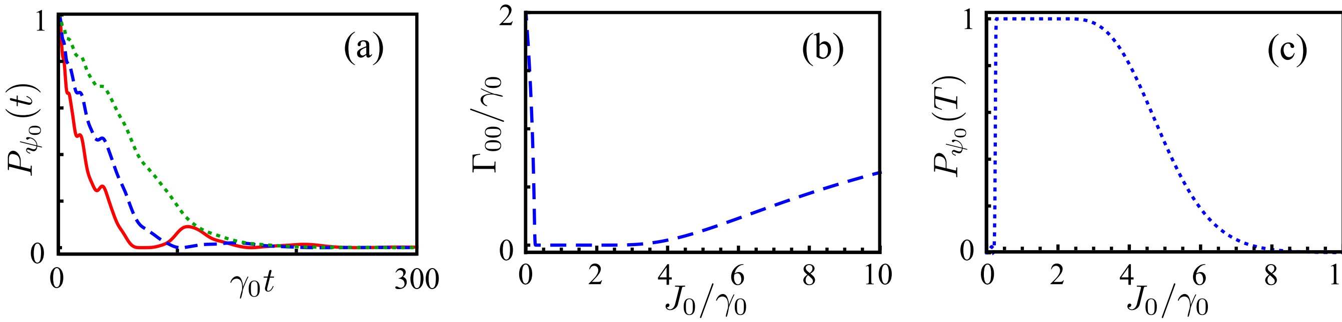

FIG. S18. (a) Population dynamics of $|\psi_0\rangle$ (the zero-energy edge state) for $J_0/\gamma_0 = 0.245$ (red-solid), 0.25 (blue-dashed) and 0.255 (green-dotted). (b) Decay rate Γ_{00} of the edge state versus J_0/γ_0. (c) Population $|\psi_0|^2$ of the edge state at time $T = 10/\gamma_0$. Here, we consider $\varphi = 0.3\pi$ and $N = 21$.

(IV-B) Accessing DTPT via multi-emitter dynamics

Detection of topological phase transitions is an important task in studying topological matter. The topological phase transition can be characterized by changes in the topological invariants, e.g., Berry phase and Chern number. The Berry phase has been directly observed in various systems. Due to the bulk-edge correspondence, a topological phase transition leads to the appearance or disappearance of edge states. In our system, *the edge states exhibit different dissipative properties around the dissipative topological phase transition.* This feature can be beneficial for the experimental observation of the topological criticality.

As we studied in the main text, the critical point $\gamma_0 = 4J_0$ represents the dissipative topological phase transition. Due to the different dissipative properties of the edge state near the critical point, we use multi-emitter population dynamics to probe the dissipative topological phase transition.

In Fig. S18(a), we show the population dynamics of the edge state in the emitter array $N = 21$. For $J_0/\gamma_0 = 0.245$ (red-solid), the population displays fast decay and oscillations. At the critical point $J_0/\gamma_0 = 0.25$, the population shows slower decay (blue-dashed). *The population revival is suppressed for the weak correlated decays between the edge state and the bulk states.* In the topological phase at $J_0/\gamma_0 = 0.255$, *the edge state has exponential decay without population oscillations.* In finite systems, the weak emitter-environment coupling, i.e., large J_0/γ_0, leads to the increased decay rate of edge state in the topological phase ($J_0/\gamma_0 > 1/4$), as shown in Fig. S18(b). Such behavior of the edge state can be witnessed from its population. Figure S18(c) shows the population of the edge state at time $T = 10/\gamma_0$. We find that a large decay rate yields fast population relaxation of the edge state.

* yuxiliu@mail.tsinghua.edu.cn
† fnori@riken.jp

[S1] H.-P. Breuer and F. Petruccione, *The theory of open quantum systems* (Oxford University Press, New York, 2002).
[S2] L. Knoll, S. Scheel, and D.-G. Welsch, *QED in dispersing and absorbing media,* arXiv:quant-ph/0006121 (2000).
[S3] T. Ohta, S. Tanaka, I. Danshita, and K. Totsuka, *Topological and dynamical properties of a generalized cluster model in one dimension,* Phys. Rev. B **93**, 165423 (2016).
[S4] P. Y. Wen, K.-T. Lin, A. F. Kockum, B. Suri, H. Ian, J. C. Chen, S. Y. Mao, C. C. Chiu, P. Delsing, F. Nori, G.-D. Lin, and I.-C. Hoi, *Large Collective Lamb Shift of Two Distant Superconducting Artificial Atoms,* Phys. Rev. Lett. **123**, 233602 (2019).
[S5] M. Mirhosseini, E. Kim, X. Zhang, A. Sipahigil, P. B. Dieterle, A. J. Keller, A. Asenjo-Garcia, D. E. Chang, and O. Painter, *Cavity quantum electrodynamics with atom-like mirrors,* Nature **569**, 692 (2019).
[S6] Y. Chen, C. Neill, P. Roushan, N. Leung, M. Fang, R. Barends, J. Kelly, B. Campbell, Z. Chen, B. Chiaro, A. Dunsworth, E. Jeffrey, A. Megrant, J. Y. Mutus, P. J. J. O'Malley, C. M. Quintana, D. Sank, A. Vainsencher, J. Wenner, T. C. White, M. R. Geller, A. N. Cleland, and J. M. Martinis, *Qubit architecture with high coherence and fast tunable coupling,* Phys. Rev. Lett. **113**, 220502 (2014).